Available online at www.sciencedirect.com
ScienceDirect
Journal of Catalysis 243 (2006) 43–56
JOURNAL OF CATALYSIS
www.elsevier.com/locate/jcat

Flame-made Pt–Ba/Al_2O_3 catalysts: Structural properties and behavior in lean-NO_x storage-reduction

M. Piacentini [a], R. Strobel [a,b], M. Maciejewski [a], S.E. Pratsinis [b], A. Baiker [a,*]

[a] *Institute for Chemical and Bioengineering, Department of Chemistry and Applied Bioscience, ETH Zurich, Hönggerberg HCI, CH-8093 Zurich, Switzerland*
[b] *Particle Technology Laboratory, Department of Mechanical and Process Engineering, ETH Zurich, CH-8092 Zurich, Switzerland*

Received 19 May 2006; revised 7 July 2006; accepted 10 July 2006

Available online 21 August 2006

Abstract

A series of Pt–Ba/Al_2O_3 catalysts with Ba loadings in the range of 4.5–33 wt% was prepared using a two-nozzle flame spray pyrolysis method. The structural properties and activities of these catalysts in NO_x storage-reduction (NSR) were compared to corresponding standard Pt–Ba/Al_2O_3 catalysts prepared conventionally via wet impregnation. The catalysts were characterized by XRD, TEM, ESI, DRIFT, TG-MS, TPRD, and gas adsorption. Calcined flame-derived catalysts were composed of agglomerated spherical nanoparticles of alumina and Pt/barium carbonate of low thermal stability (LT-$BaCO_3$), whereas barium carbonate of high stability (HT-$BaCO_3$) was absent. In contrast, in the corresponding conventionally prepared catalysts, the Ba-containing phases were composed of BaO, LT-$BaCO_3$, and HT-$BaCO_3$. DRIFTS measurements of CO adsorption revealed distinct differences in the distribution of CO chemisorbing sites on Pt particles depending on the preparation method applied. The CO:Pt ratio varied between 0.8 and 0.7 depending on the Ba loading and the preparation method. Decreased Pt dispersion at higher Ba loadings was observed for the wet-impregnated catalysts, whereas Pt dispersion increased only slightly at higher Ba loadings for the flame-made catalysts. The structural differences of flame-made and conventionally prepared catalysts affected strongly their NO_x storage efficiency. Investigation of the behavior of the catalysts in NSR showed that the larger Ba/Al_2O_3 interface existing in conventionally prepared catalysts results in a higher NO_x storage efficiency of these catalysts at Ba loadings up to ca. 17 wt%, whereas the absence of the HT-$BaCO_3$ phase in flame-made catalysts lead to improved NO_x storage potential at higher Ba loadings.

Keywords: NO_x storage-reduction; Pt–Ba/Al_2O_3; Effect of Ba loading; Stability of Ba-containing phases; Pulse thermal analysis; Temperature programmed reaction-desorption; Barium carbonate; Barium nitrate; Flame spray pyrolysis; Two-nozzle system

1. Introduction

NO_x pollution from combustion processes has been a challenging area of environmental chemistry ever since new, more efficient engines operating under lean conditions were introduced [1,2]. NO_x storage-reduction (NSR) catalysts proposed by Toyota in 1995 [3] seem to offer the most realistic solution in terms of dynamic NO_x control. Nitrogen oxides are stored under lean conditions over an alkaline or alkaline-earth component (i.e., $BaCO_3$ or BaO) in the form of nitrates, which are then reduced to nitrogen during a short fuel-rich period [4–7]. The standard NSR catalyst is Pt–Ba/Al_2O_3 generally prepared by wet impregnation of an alumina support with aqueous solutions of barium and platinum precursors [8].

The classical NO_x storage mechanism assumes that either BaO or $BaCO_3$ species are the storage compounds [8]. Recently it has been shown that the distribution of different Ba-containing species over the support [9–14] is a crucial factor for storage efficiency [15,16], especially in the case of alumina-supported catalysts [17,18]. A detailed study of the influence of the Ba loading in standard Pt–Ba/Al_2O_3 revealed the presence of different Ba-containing phases in the conventional Pt–Ba/Al_2O_3 NSR catalyst. The existence of different Ba-containing phases was traced to varying interaction of the Ba species with the alumina support [15]. In a preceding study we described the activity of each of these Ba-containing phases in the NO_x storage process and proposed a direct relation be-

* Corresponding author. Fax: +41 1 632 1163.
E-mail address: baiker@chem.ethz.ch (A. Baiker).

0021-9517/$ – see front matter
doi:10.1016/j.jcat.2006.07.005

tween thermal stability and storage potential of the diverse $BaCO_3$ phases [16]. $BaCO_3$ in intimate contact with the support (LT-$BaCO_3$), partially decomposing to BaO at low temperatures, was found to be the most active Ba-containing phase in the NO_x storage process, whereas bulk-like $BaCO_3$ decomposing at higher temperatures (HT-$BaCO_3$) represents a limiting factor for NO_x storage efficiency. Recently our findings were confirmed by Chen et al. [13], who identified two different Ba-NO_x species with different thermal stabilities, resulting from the thermal decomposition of alumina-supported $Ba(NO_3)_2$.

Intrigued by our earlier findings, we attempted to prepare Pt–Ba/Al_2O_3-based catalysts with limited formation of larger $BaCO_3$ clusters, accompanied by HT-$BaCO_3$ formation [15]. Among the various preparation methods, flame spray pyrolysis (FSP) was chosen, based on some of its unique features [19]. This method, based on dispersing and igniting combustible precursor solutions [20], gives access to all kinds of metal-containing nanoparticles [19]. Such flame-made (FM) materials are characterized by a relatively high surface areas [21] due to the external surface of the nanoparticles and the nonporous structure generally improving thermal stability [21,22].

The conventional single-nozzle FSP process has some inherent limitations in controlling the distribution of two or more components in the material, as in the case of mixed metal oxides, resulting in poor NSR catalysts [23]. Recently, we have shown that a two-nozzle flame process adds further flexibility in setting of flame parameters and provides better control of particle mixing at the nanolevel in the Pt–Ba–Al system [23].

Consequently, intrigued by the obvious advantages of the two-nozzle flame process, we prepared a series of FM Pt–Ba/Al_2O_3 catalysts with Ba loadings in the range of 4.5–33 wt% and compared their structural properties and behavior in NO_x storage reduction to those of corresponding standard Pt–Ba/Al_2O_3 catalysts prepared by wet impregnation (WI).

2. Experimental

2.1. Catalyst preparation

Two sets of NO_x storage-reduction catalysts, with the standard formulation Pt–Ba/Al_2O_3, were prepared by means of two different methods: the incipient wetness technique (denoted as WI catalysts) and the flame spray pyrolysis (denoted as FM catalysts). The WI samples were prepared using $Pt(NH_3)_2(NO_2)_2$ and $Ba(CH_3COO)_2$ as precursors, and commercial γ-Al_2O_3 (BET surface area = 210 $m^2\,g^{-1}$) as a support. The detailed preparation procedure has been described previously [15]. As-prepared samples with a Pt content of 1 wt% were dried for 12 h at 80 °C and then calcined at 500 °C for 2 h, all in air. After calcination, the samples were impregnated with $Ba(CH_3COO)_2$ solutions affording nominal Ba loadings of 4.5, 9, 16.7, 22, and 28 wt%, and then dried for 12 h in air at 80 °C. Before each experiment, the samples were calcined in situ with a temperature ramp of 10 °C min^{-1} up to 500 °C.

The setup for flame synthesis of Pt–Ba/Al_2O_3, described in detail previously [23], consisted of two separate FSP nozzles, with the angle between them fixed at 120° and the internozzle distance between the angle tip and each nozzle center fixed symmetrically at 6 cm. The Al- and Pt/Ba-containing precursor solutions were fed separately through the two nozzles. The Al precursor consisted of aluminum(III) tri-*sec*-butoxide (Alfa Aesar, 95%) dissolved in a 2:1 vol% mixture of diethylene glycol monobutyl ether (Fluka, 98%) and acetic anhydride (Riedel de-Haën, 99%). For the Pt/Ba precursor mixture, barium(II) 2-ethylhexanoate (75% in 2-ethylhexanoic acid; Alfa Aesar, 99.8%) and platinum(II) acetylacetonate (Strem, 98%) were dissolved in ethanol (Alcosuisse, 98%). The Al concentration was maintained at 0.5 mol L^{-1} for all experiments. The platinum and barium concentrations were adjusted to afford a Pt content of 1 wt% and nominal Ba loadings of 4.5, 9, 16.7, 23, and 33 wt%. The flames were operated in open air environment, reaching maximum flame temperatures of up to 2500 °C [20]. Liquid and gas flow rates were as described previously [23].

Table 1
Nominal composition of WI and FM Pt–Ba/Al_2O_3 catalysts: Ba and Pt loading in wt%

WI Pt–Ba/Al_2O_3		FM Pt–Ba/Al_2O_3	
Ba (wt%)	Pt (wt%)	Ba (wt%)	Pt (wt%)
4.5	0.94	4.5	0.94
9	0.91	9	0.91
16.7	0.83	16.7	0.83
22	0.77		
		23	0.76
28	0.71		
		33	0.66

For comparison, Pt–Ba/Al_2O_3 powder (with a relative formulation of 1:20:100) was also produced by one-nozzle FSP with a precursor feed rate of 5 ml min^{-1} and an oxygen dispersion gas flow rate of 5 L min^{-1}. In that precursor, the solutions of aluminum(III) tri-*sec*-butoxide, barium(II) 2-ethylhexanoate (Aldrich, 98%), and platinum(II) acetylacetonate were dissolved in toluene (Al = 0.5 mol L^{-1}).

Both the WI and FM samples are designated as Pt–Ba(x), where x denotes the nominal wt% of Ba in the sample, for example, Pt–Ba(22.0). The relative loading of Pt was kept constant (i.e., Pt(1)–Ba(x)–Al_2O_3(100)); therefore, the absolute Pt content decreases with increasing Ba loading to a minimal value of ca. 0.7 wt% for WI Pt–Ba(28) and 0.6 wt% for FM Pt–Ba(33) [15]. Table 1 lists the composition of the catalysts used in this study.

2.2. Catalyst characterization and NO_x storage-reduction tests

Specific surface areas (S_{BET}), specific pore volumes (V_p), and average pore diameters ($\langle d\rangle = 4V_p/S_{BET}$) of the calcined supports and supported Pt–Ba samples with different Ba loadings were determined by nitrogen adsorption–desorption measurements at 77 K using a Micromeritics Tristar 3000 instrument. Pore size distributions (not shown) were calculated using the Barrer–Joyner–Halenda method [24]. The assessment of microporosity was made using t-plot constructions [25].

Powder X-ray diffraction (XRD) patterns of calcined WI samples were recorded with a Siemens D5000 powder X-ray diffractometer using the CuK_α radiation in step mode between 10 and 80° 2θ with a step of 0.01° and 2 s step^{-1}. XRD analysis of FM materials was carried out on a Bruker D8 advance diffractometer in step mode (2θ = 15°–75°) with a step size of 0.04° and a scan speed of 0.48° min^{-1}.

For transmission electron microscopy (TEM), the calcined material was dispersed in ethanol and deposited onto a perforated carbon foil supported on a copper grid. The investigations were performed on a Tecnai F30 microscope (FEI [Eindhoven]; field emission cathode, operated at 300 kV). TEM images were recorded with a slow-scan CCD camera. An energy filter (Gatan imaging filter [GIF]), which is installed below the Tecnai F30, allows the recording of element-specific images (elemental maps) of barium (Ba-L edge at an energy loss of 781 eV) by means of the electron spectroscopic imaging (ESI) technique [26].

CO-pulse chemisorption was performed by injecting pulses (0.35 ml) of 10% CO/He into 5% H_2/Ar at 40 °C on a Micromeritics Autochem II 2920 instrument. A mass spectrometer (Pfeiffer Vacuum, Thermostar) was used to analyze the off-gas and derive the amount of chemisorbed CO. Before CO chemisorption, all samples were freshly pretreated to remove impurities as follows: Samples were first heated in 10% O_2/He up to 500 °C (10 °C min^{-1}) and maintained for 30 min at 500 °C, then cooled in He to 350 °C to prevent mixing of O_2 and H_2. Complete reduction of PtO_x sites was then achieved by exposing the samples to 5% H_2/Ar for 30 min at 350 °C. Subsequently, the samples were kept for 30 min at 350 °C before cooling in He to 40 °C. Preferential chemisorption of CO instead of H_2 on the Pt sites can be assumed [27–29].

DRIFTS analysis of CO chemisorption was performed on a Bruker IFS 55 spectrometer. A Praying Mantis diffuse reflection attachment (DRA) coupled with a HVC-DRP2 reaction chamber (Harrick) was used. Before each analysis, all samples were freshly pretreated following the procedure previously described for CO chemisorption. Gas flow was kept at 10 ml min^{-1}, and pure H_2 was used in the reducing step. For determination of metal dispersion, the adsorption stoichiometry defined CO molecules per surface Pt atom was calculated, taking into account the relative proportion of linear-CO and bridged-CO as shown by DRIFTS analysis. CO:Pt ratios were between 0.8 and 0.7 depending on the catalyst preparation method and the Ba loading.

Thermogravimetry (TG) combined with mass spectrometry (MS) was performed on a Netzsch STA 409 thermoanalyzer connected to a valve device enabling pulse thermal analysis (Pulse TA®). This setup [30] allows the injection of controlled amounts (0.5–5 ml) of probe gas into a carrier gas stream (here fixed at 50 N cm^3 min^{-1}) flowing through the thermoanalyzer. The composition of the gas phase was monitored by a ThermoStar Pfeiffer Vacuum GSD 301 O1 mass spectrometer, which was connected to the thermoanalyzer by a heated (ca. 200 °C) stainless steel capillary.

Application of mass spectrometry in analyzing the mixtures containing both NO and NO_2 is biased by the fact that the main m/z signals are the same for both gases (m/z = 30). This problem has been circumvented by careful calibration of the mass spectrometer (injection of NO and NO_2) and determination of the specific fragmentation pattern. This procedure allowed estimation of the amount of NO_2 evolved during TPRD experiments. Note that the measured concentration of NO_2 was generally ca. two orders of magnitude lower than that of NO.

Before each experiment (i.e., TG-MS, TPRD, NO_x storage, and NSR), the samples were calcined in situ in 20 vol% O_2/He at 500 °C (at a temperature ramp of 10 °C min^{-1}) for 2 h. Cooling was conducted in controlled atmosphere as well.

TPRD experiments were carried out with 20 mg samples in He with a heating rate of 10 °C min^{-1}. NO_x storage tests were performed at 300 °C in a 5 vol% O_2/He atmosphere, with repeated 1 cm^3 NO pulses injected into a carrier gas stream until saturation (maximal mass uptake) was reached.

NO_x storage-reduction (NSR) in an inert atmosphere was performed at 300 °C in He with 1 cm^3 C_3H_6 pulses injected alternatively with a certain number of 2 cm^3 NO/3 cm^3 O_2 pulses. The injection of NO/O_2 results in a mass gain. The reduction by propene (marked by arrows in Figs. 13 and 14) was done after one and three pulses of NO/O_2 and finally after saturation of active Ba sites was reached, that is, after five (Fig. 13A) or six (Figs. 13B–13D) NO/O_2 pulses. NSR in the presence of oxygen was tested at 300 °C in an 8000 ppm O_2/He atmosphere.

3. Results

3.1. Structural and chemical properties of catalysts

Wet-impregnated Pt–Ba/Al_2O_3 (WI) and flame-made (FM) catalysts were characterized with respect to their surface area, morphology, platinum and barium distribution, and crystallinity. Special attention was given to the elucidation of structural features that can be directly related to the innovative preparation method, involving two-nozzle FSP.

The BET surface areas, S_{BET}, of non-Ba-containing samples (Pt/Al_2O_3) were 190 m^2 g^{-1} for the WI samples and 155 m^2 g^{-1} for the FM samples. Ba loading led to a decrease in surface area irrespective of the preparation method applied. However, the BET surface area of FM catalysts was less affected by high Ba loading than that of corresponding WI catalysts, as reflected by an S_{BET} of 118 m^2 g^{-1} for FM Pt–Ba(33) compared to 104 m^2 g^{-1} for WI Pt–Ba(28) (Fig. 1). N_2 adsorptions/desorption isotherms of the WI samples indicate a significant mesoporosity [average pore diameters, $\langle d \rangle$, of ca. 10 nm Pt–Ba(4.5)] characteristic for material with tubular-shaped pores open at both ends [18,31] (Fig. 2, inset). The partial blocking of these pores by the deposited Ba-containing component resulted in a decrease of S_{BET} and of the cumulative pore volume with increasing Ba loading. FM catalysts (Fig. 2) show the typical hysteresis loop for flame-synthesized materials composed of nonporous primary nanoparticles [21].

The specific morphology of FM catalysts results in a smaller Ba/Al_2O_3 interface in the FM than in the WI materials. Results of TEM analysis combined with ESI characterizing the morphology of WI Pt–Ba(28) (left column) and FM Pt–Ba(33)

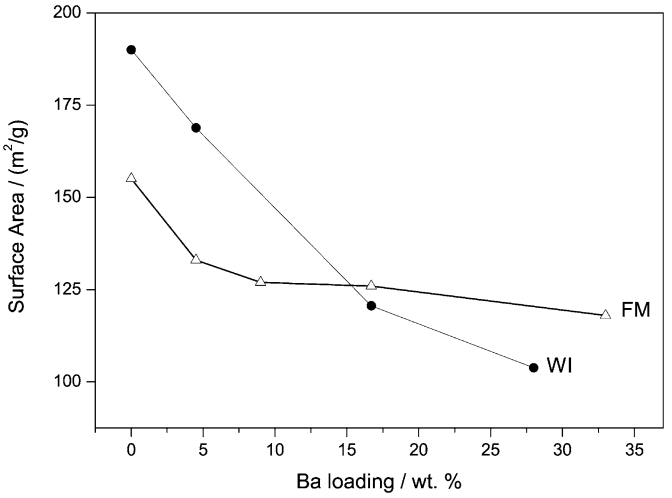

Fig. 1. Influence of Ba loading on the BET surface area of calcined Pt–Ba/Al_2O_3 catalysts prepared by wet impregnation (WI) and by flame spray pyrolysis (FM).

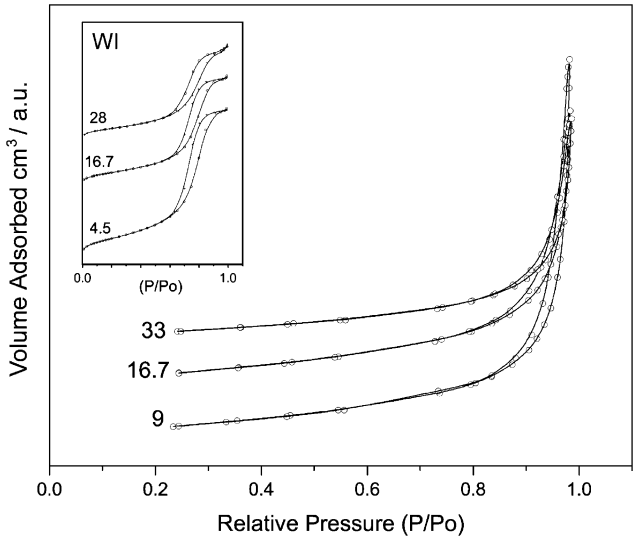

Fig. 2. Nitrogen adsorption–desorption isotherms of calcined WI (inset) and FM catalysts as a function of the Ba loading marked in wt% on the curves.

catalysts (right column) are presented in Fig. 3. Deposition of Ba via wet impregnation of the Pt/Al_2O_3 support (WI catalysts) afforded relatively large agglomerates of Ba-containing species (ca. 80–100 nm) in high Ba-loaded samples (Fig. 3, left middle). The thickness of the Ba-containing domains increased with increasing Ba loading. In contrast, FM catalysts (Fig. 3, right column), with Pt, Al, and Ba organic precursors burned together, were composed of relatively small spherical particles of alumina (Fig. 3, right bottom) in intimate contact with slightly larger particles of Ba-containing species (ca. 30 nm). These characteristic features were observed virtually independent on the Ba loading. Note that in FM materials, a large fraction of the alumina surface was not covered by the Ba component.

Fig. 4, showing high-resolution STEM images of the same samples, indicates that in FM catalysts Pt is observed on both Ba-containing (spherical particles of ca. 34 nm, encircled) and Al_2O_3 particles, as confirmed by ESI analysis. Thus, we may conclude that the FM catalysts are composed of primary spherical particles of alumina and barium carbonate that are aggregated to larger particles (Scheme 1). Platinum is dispersed on both types of primary particles. This morphology is distinctly different than that of WI catalysts, where the Ba-containing phase is deposited on the alumina support particles.

CO pulses over preactivated catalysts showed that Ba loading affected the specific CO uptake differently. With the WI catalysts, the CO uptake decreased strongly with Ba loading, whereas with the FM catalysts, CO uptake increased slightly with Ba loading (Fig. 5, inset). In situ DRIFTS analysis showed that both linear-CO (L-CO) (1970, 2016, 2060 and 2076 cm^{-1}) and bridged-CO (B-CO) (1790 and 1810 cm^{-1}) species were present (Fig. 5). The relative abundance of these species depended on the preparation method and on the Ba loading. The significant concentration of B-CO species indicates a CO:Pt ratio < 1. The adsorption stoichiometry derived from the ratio of the signal areas of L-CO and B-CO species varied between 0.7 and 0.8 depending on the preparation method and the Ba loading. This stoichiometry agrees well with that found recently by Dawody et al. [32].

The crystallinity of Ba-containing phases was investigated by means of XRD (Fig. 6). $BaCO_3$ reflections were observed already at the low Ba loading of Pt–Ba(4.5) in FM catalysts, whereas in WI samples, crystalline $BaCO_3$ appeared only above a Ba loading of ca. 16 wt% due to the formation of high-temperature (HT)-$BaCO_3$ phase [15]. However, after prolonged exposure to ambient atmosphere reflections indicative of crystalline LT-$BaCO_3$ were also found in low Ba-loaded WI samples [15]. Both orthorhombic (witherite) and monoclinic $BaCO_3$ [33] were present in freshly calcined samples of WI and FM catalysts, but the relative concentration of monoclinic $BaCO_3$ was significantly higher in FM catalysts [34] (Fig. 6). Irrespective of the preparation method used, monoclinic $BaCO_3$ progressively transformed into the more stable orthorhombic phase [34–36].

3.2. Thermal stability of supported $BaCO_3$

The influence of the different preparation methods on the thermal stability of supported barium carbonate was investigated by means of TPRD measurements. Fig. 7 shows CO_2 evolution traces recorded during heating the FM Pt–Ba(16.7) sample in He to 900 °C with a rate of 10 °C min^{-1}. Three CO_2 evolution peaks (mass spectrometric signal $m/z = 44$) were observed, closely resembling those monitored during TPRD of corresponding WI catalyst calcined ex situ and exposed to ambient atmosphere (Fig. 7, inset B). From a qualitative comparison to the results of TPRD of WI catalyst calcined in situ (Fig. 7, inset A), it seems reasonable to assume that only part of the totally evolved CO_2 (i.e., the signal centered at ca. 650 °C) accounts for the presence of LT-$BaCO_3$ (Fig. 7, dotted line) [15]. The first two CO_2 peaks can be attributed to the decomposition of very unstable carbonates (CO_2 evolution centered at ca. 380 °C) formed during exposure to

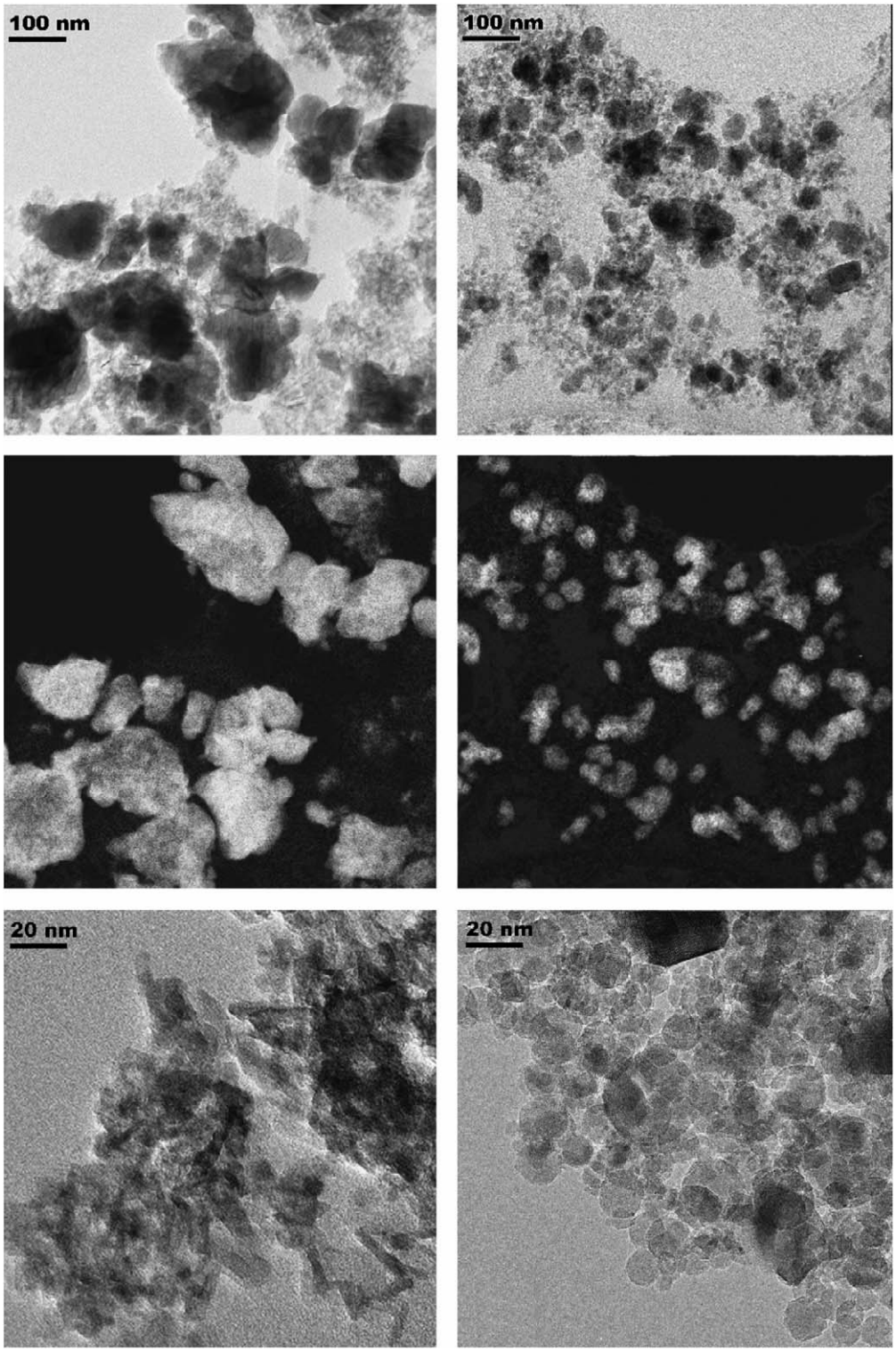

Fig. 3. Transmission electron micrographs (top and bottom) and ESI mapping of Ba component (middle) in alumina supported WI Pt–Ba(28) (left column) and FM Pt–Ba(33) (right column) showing major structural differences. Note that the scale of TEM images on top and bottom is different. Bottom images show higher resolution of the structural features of the main component alumina (support).

atmosphere after synthesis and to desorption of physisorbed CO_2 from the catalyst. The contribution of the alumina surface (peak centered at ca. 170 °C) to the physisorption of CO_2 must be taken into account particularly for FM materials due to a higher relative fraction of the uncovered alumina surface compared to WI materials, as indicated by the ESI-TEM results.

It should be stressed that in the flame synthesis, the high CO_2 in the flame results in higher relative concentration of LT-$BaCO_3$, whereas the BaO concentration is very low (inner core

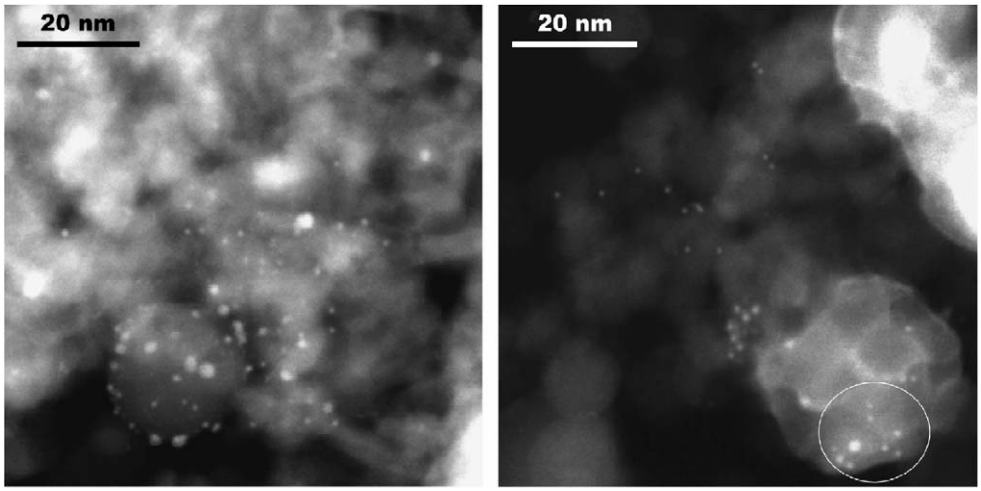

Fig. 4. High-resolution STEM images showing Pt particles (bright spots) in WI Pt–Ba(28) (left) and FM Pt–Ba(33) (right) catalysts. In the FM sample (right), Pt particles are discernible on both, Ba-containing (encircled) and alumina, particles. Different phases have been identified by ESI.

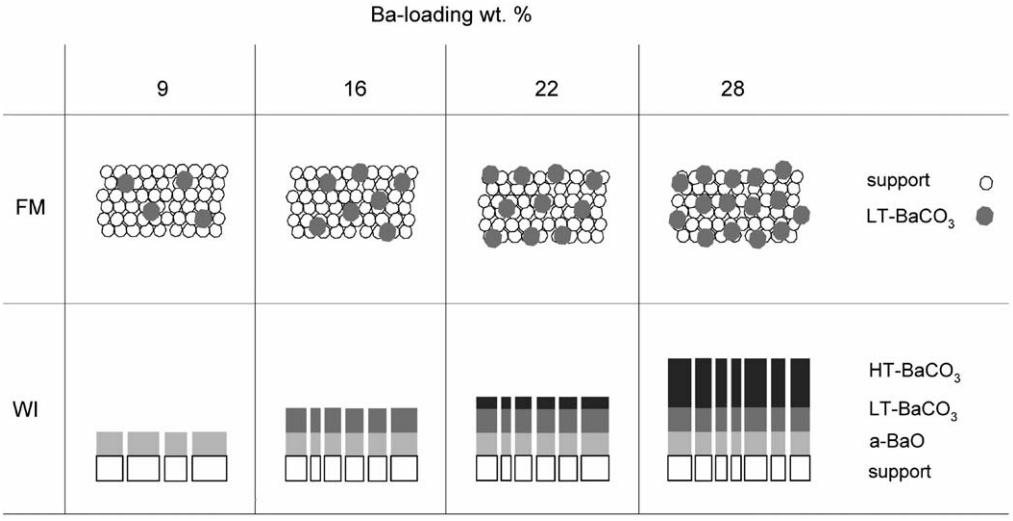

Scheme 1. Schematic presentation of the difference in the main structural features of WI and FM catalysts, as suggested from TEM and ESI analysis (cf. Fig. 3).

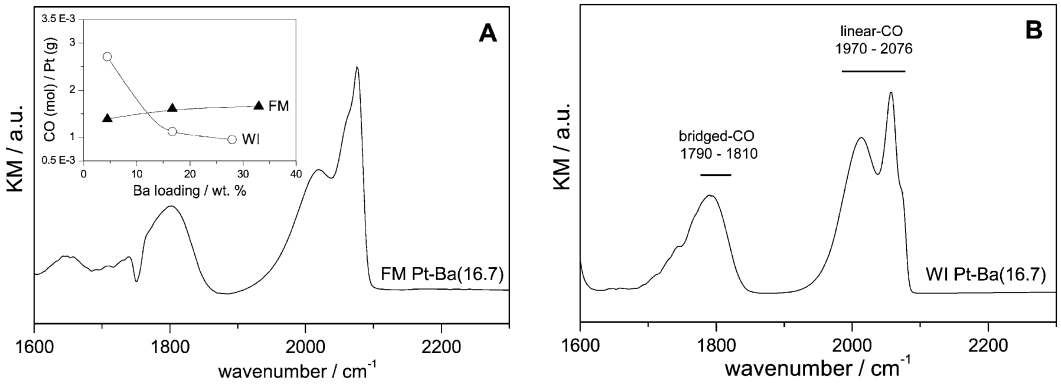

Fig. 5. In situ DRIFT analysis of Pt–Ba/Al_2O_3: spectra taken during CO chemisorption at 40 °C on (A) FM Pt–Ba(16.7) catalyst and (B) WI Pt–Ba(16.7) catalyst. Assignment of the bands: 1970, 2010, 2060, 2076 cm^{-1} linear-CO; 1810 and 1790 cm^{-1} bridge-CO. The inset shows the moles of CO chemisorbed per gram of Pt versus Ba loading in WI (○) and FM (▲) catalysts.

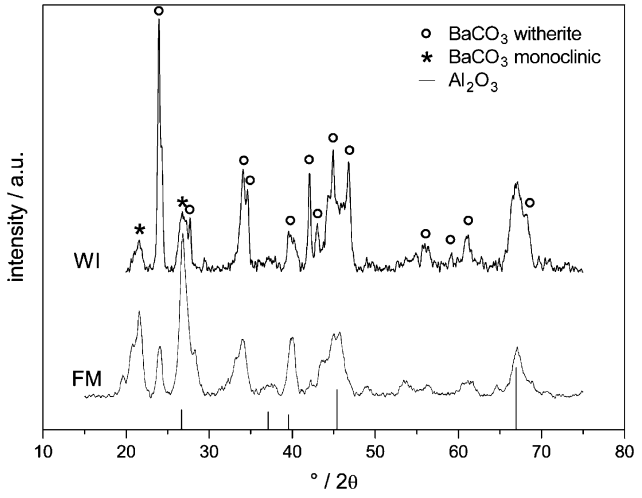

Fig. 6. XRD patterns of calcined WI Pt–Ba(22) and FM Pt–Ba(23) samples. (○) $BaCO_3$ witherite: JCPDS 44-1487; (∗) $BaCO_3$ monoclinic: JCPDS 41-631; γ-Al_2O_3: JCPDS 29-063.

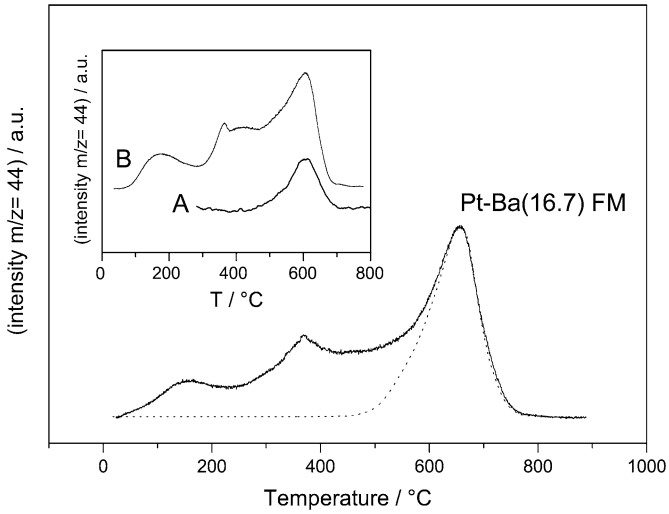

Fig. 7. TPRD CO_2 evolution profiles of FM Pt–Ba(16.7) catalyst: experimental $m/z = 44$ signal (solid line), estimated LT-CO_2 evolution profile (dotted line). The inset shows TPRD CO_2 evolution profiles of WI sample Pt–Ba(9): (A) freshly calcined, (B) calcined and stored for 4 months at ambient atmosphere.

of $BaCO_3$ particles). Fig. 8 presents the amount of barium carbonate in the form of LT-$BaCO_3$ versus Ba loading derived from TPRD results for FM and in situ calcined WI catalysts. The concentration of Ba in the form of LT-$BaCO_3$ is much less dependent on the Ba loading in the FM catalysts than in the WI catalysts, where it progressively increases with Ba loading. The FM catalysts showed no HT-$BaCO_3$ even at very high Ba loading, whereas HT-$BaCO_3$ was present in WI catalysts at Ba loading >16.7 wt%.

3.3. NO_x storage

The influence of the different distributions of BaO, LT-$BaCO_3$, and HT-$BaCO_3$ in FM and WI catalysts on the efficiency of NO_x storage was studied. Because HT-$BaCO_3$ was

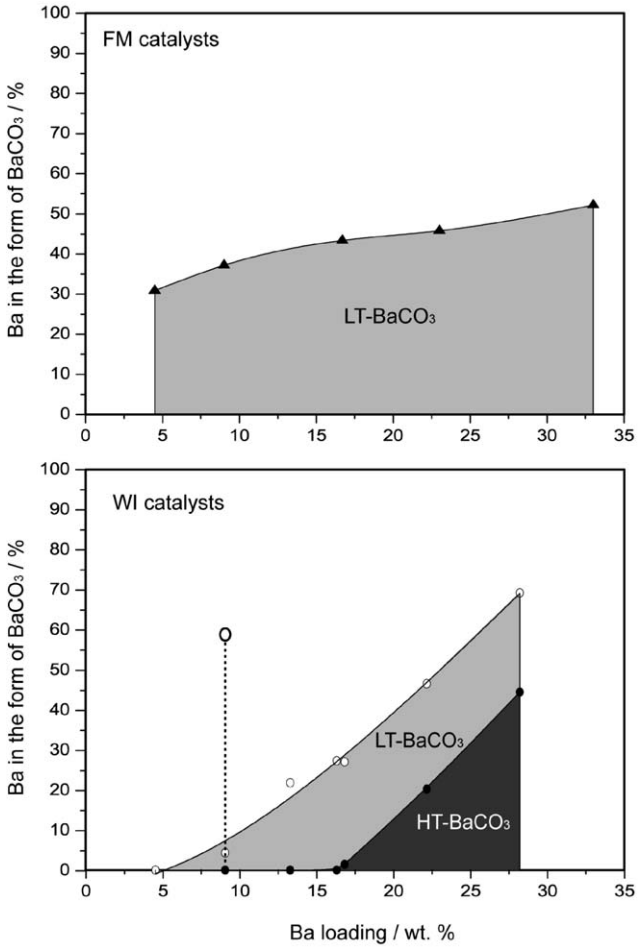

Fig. 8. Fraction (wt%) of Ba-containing phases in FM (top) and calcined WI (bottom) catalysts present in the form of LT-$BaCO_3$ (light grey) and HT-$BaCO_3$ (dark grey) as a function of Ba loading. Larger open circle (O) at ca. 58% indicates the corresponding content of $BaCO_3$ in WI Pt–Ba(9) catalyst calcined and stored for 4 months in ambient atmosphere.

shown to be the major factor responsible for the limited NO_x storage efficiency in the WI catalysts [16], the absence of this phase in the FM catalysts should result in a better performance at higher Ba loadings. To test this hypothesis, catalysts calcined up to 500 °C were exposed at 300 °C to NO pulses in 5 vol% O_2/He atmosphere until saturation of the active storage sites was achieved.

When exposing $BaCO_3$-containing catalysts to NO/O_2 NO_x storage occurs mainly according to the following global reaction:

$$BaCO_3 + 2NO + \frac{3}{2}O_2 \rightarrow Ba(NO_3)_2 + CO_2.$$

Therefore, the mass changes observed during this process resulted from two counteracting processes: (i) a mass loss due to CO_2 evolution and (ii) a mass gain due to barium nitrate formation. A direct comparison of the TG curves recorded during NO_x storage is presented in Fig. 9. Note that saturation of the active sites by NO_x was approached in the FM catalysts after the third NO pulse, whereas many more NO pulses were required for the WI catalysts. The monitored MS signal $m/z = 44$ (not shown) revealed that the end of evolution of

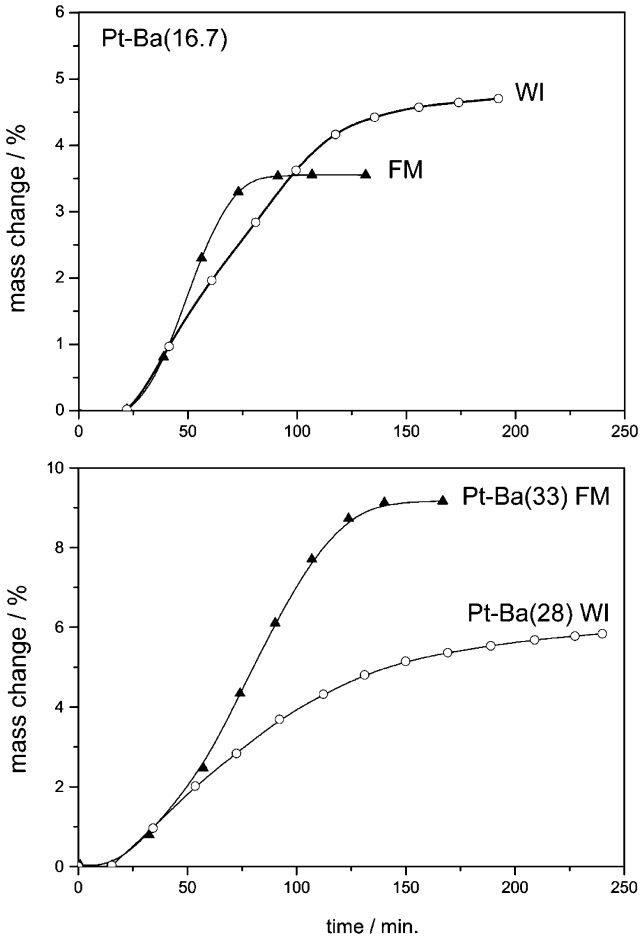

Fig. 9. NO_x storage over differently Ba-loaded WI and FM catalysts: TG mass-gain signals registered during 1 cm^3 NO pulses at 300 °C in 5 vol% O_2/He atmosphere.

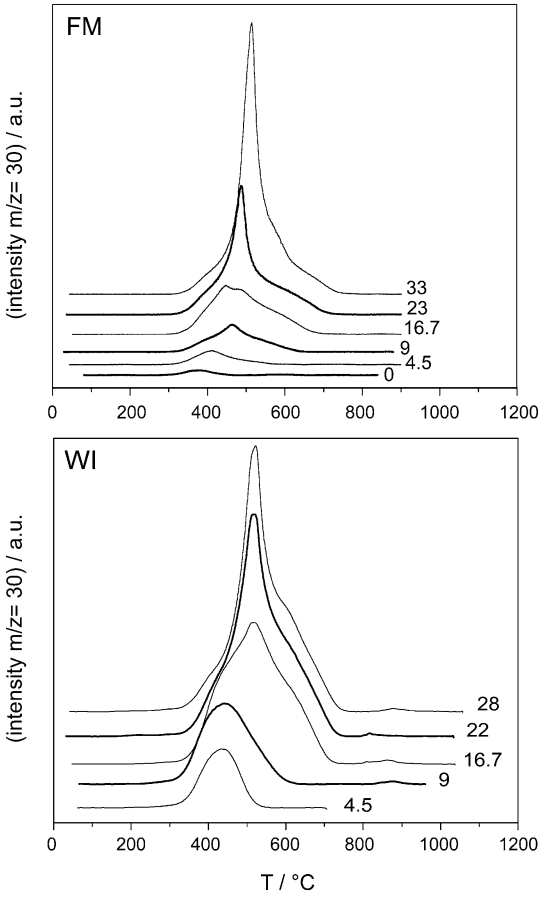

Fig. 10. TPRD NO evolution profiles of FM and WI catalysts after NO_x storage on different Ba-loaded samples (Ba loading in wt% is marked on curves).

CO_2 corresponded to the end of the mass change for the FM catalysts. This indicated a correlation between the saturation of active sites and the consumption of the LT-$BaCO_3$ phase. The same relationship between TG and CO_2 signals was previously observed for WI samples [16]. FM samples showed similar behavior even at higher Ba loadings (Fig. 9, bottom).

The results are in agreement with the specific NO_x storage efficiency of the LT-$BaCO_3$ phase described in detail in our previous work on WI catalysts [16]. Further indication of the importance of the LT-$BaCO_3$ phase in FM materials emerges from a comparison of the NO_x storage capacity of FM materials [Pt–Ba(16.7)] prepared by applying one nozzle (FM1) or two nozzles (FM2) in the FSP [23]. The FM1 sample contained no LT-$BaCO_3$ and had a very poor NO_x storage capacity, basically resembling that of Pt/Al_2O_3, whereas the FM2 sample had a high LT-$BaCO_3$ content and a high NO_x storage capacity.

Quantification of the NO stored on differently Ba-loaded samples was achieved by TPRD (Fig. 10). Similar $m/z = 30$ traces were observed for the FM and WI samples.

Active Ba sites present in the samples were derived from $Ba(NO_3)_2$ content, in turn quantified by determination of the amount of NO evolved during TPRD as NO_x species are stored as nitrates once saturation of active sites is achieved [16,35,37]. The form of active Ba-containing species in the NO_x storage process is shown in Fig. 11. In the FM catalysts, ca. 80% of active Ba was in the form of LT-$BaCO_3$, whereas in the WI catalysts, the fraction of LT-$BaCO_3$ increased with increasing Ba loading, as shown in Fig. 8. The remaining active Ba in WI catalysts existed in the form of BaO [$Ba(OH)_2$] and HT-$BaCO_3$.

The amount of NO (in mg) stored per mg of catalyst is shown in Fig. 12. Fig. 12 also shows the NO_x storage efficiency of the FM and WI catalysts with different Ba loadings, expressed as percentage of Ba species active in NO_x storage versus Ba loading. These results confirm our working hypothesis assuming that the major differences in NO_x storage capacity at higher Ba loadings are due to the absence of the limiting influence of HT-$BaCO_3$ in the FM catalysts.

3.4. Reduction of stored NO_x

The reduction of stored NO_x species was carried out by pulsing of C_3H_6 at 300 °C over NO_x-saturated samples. C_3H_6 pulses were injected into the system after a certain number of NO/O_2 pulses (i.e., 1, 3, and up to active NO_x storage site saturation [Fig. 13A]). Two sets of experiments were performed under different conditions. A first set of NSR cycles was per-

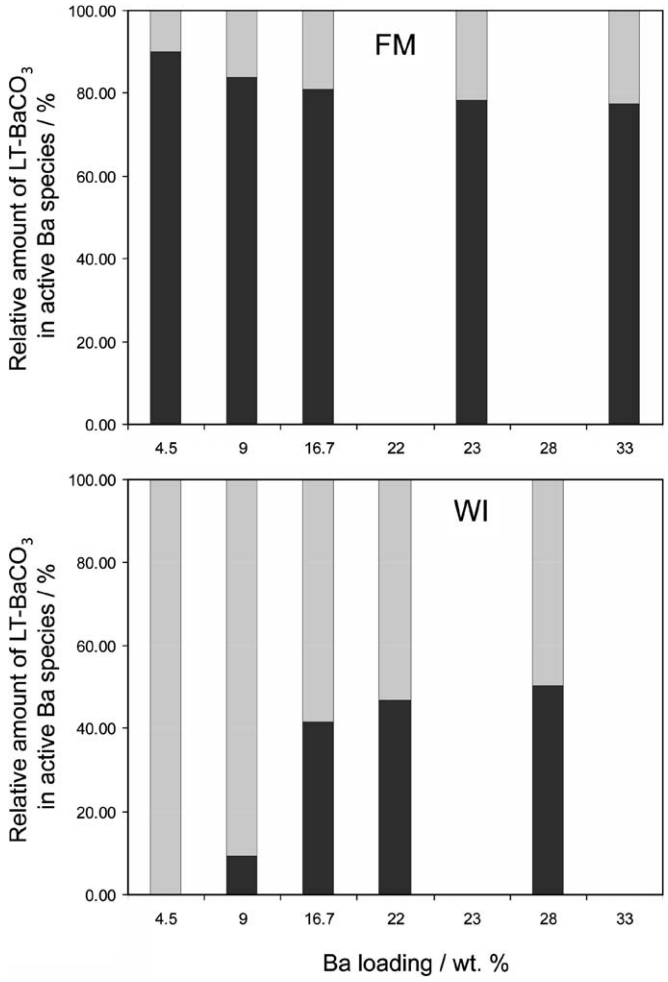

Fig. 11. Relative abundance of LT-$BaCO_3$ (dark grey) in all Ba species involved in NO_x storage as a function of Ba loading.

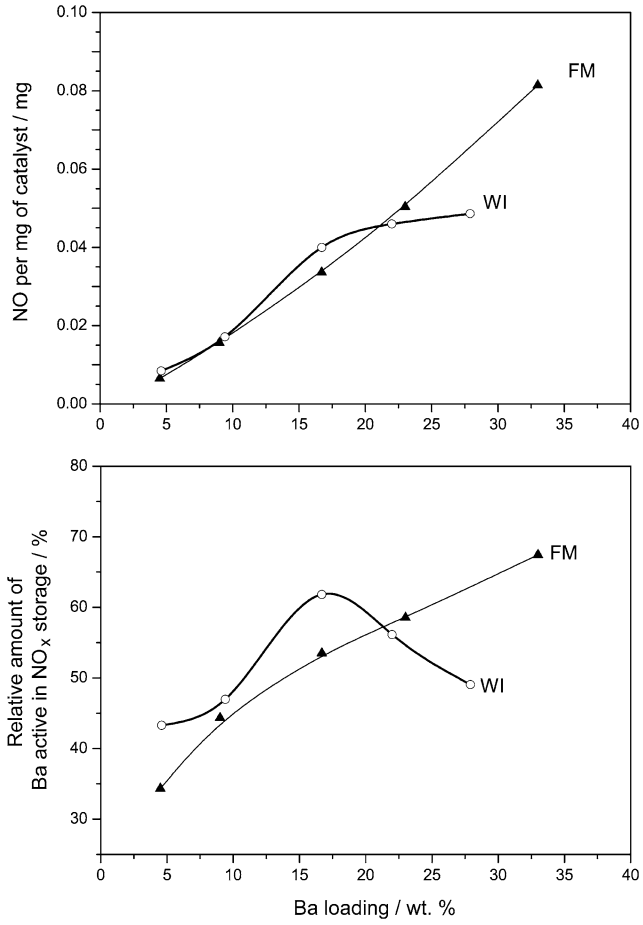

Fig. 12. NO_x storage efficiency of FM and WI Pt–Ba/Al_2O_3 catalysts: mg of NO stored per mg of catalysts (top). Ratio of Ba-containing species involved in NO_x storage to total amount of Ba species as a function of Ba loading (bottom).

formed in pure He as carrier gas (Figs. 13A and 13B); then in a second set of NSR cycles, 8000 ppm of O_2 was introduced into the carrier gas to evaluate the influence of oxygen on the reducibility of stored NO_x species (Figs. 13C and 13D). In both cases, reduction of stored NO_x species was monitored by the TG signals indicating a significant rapid mass loss on injection of C_3H_6 pulses. The presence of oxygen in the gas stream decreased the reducing effect of propene on the stored NO_x species; however, under both atmospheres, repeated C_3H_6 pulsing allowed an almost complete reduction of previously formed barium nitrate. Moreover, under both atmospheres, the storage reduction activity was similar for the FM and WI catalysts even after repeated NSR cycles (not shown).

For very high Ba loadings (i.e., when approaching the maximal NO_x storage capacity), a clear limitation in the reduction activity of the catalysts was observed (Fig. 14). This limitation was more prominent in the FM materials. At high Ba loading, TG traces indicated that WI Pt–Ba(28) was still active (Fig. 14A), whereas the FM catalyst with the highest loading [Pt–Ba(33)] showed a substantial decrease in reduction activity (Fig. 14B). Subsequent TPRD experiments confirmed that a large amount of NO_x-containing species was still present in the FM sample after the reduction (Fig. 14C).

3.5. Regeneration of supported $BaCO_3$ phases after NSR

TPRD performed after reduction of variably Ba-loaded WI and FM catalysts indicated a change in the distribution of the $BaCO_3$ phases compared to that in corresponding fresh in situ calcined samples (Figs. 15 and 16). Fig. 15 shows the respective formation, disappearance, and reconstruction of VLT-, LT- and HT-$BaCO_3$ phases during the calcination, storage, and reduction processes for the WI Pt–Ba(22)/Al_2O_3 catalyst. Formation of VLT-$BaCO_3$ during the storage step has been explained in detail previously [16], whereas its formation during reduction was due to the reaction of active BaO with CO_2 originating from C_3H_6 oxidation during pulses at 300 °C. TPRD CO_2 profiles after reduction, recalling those obtained during TPRD experiments of calcined samples, are shown for other WI and FM catalysts in Fig. 16. The relative concentration of $BaCO_3$ decomposing below 800 °C in WI indicates that part of the active BaO was converted to LT-$BaCO_3$. Interestingly, FM Pt–Ba(33) showed only partial regeneration of $BaCO_3$ phases during the reduction process (due to a diminished reduction activity) and

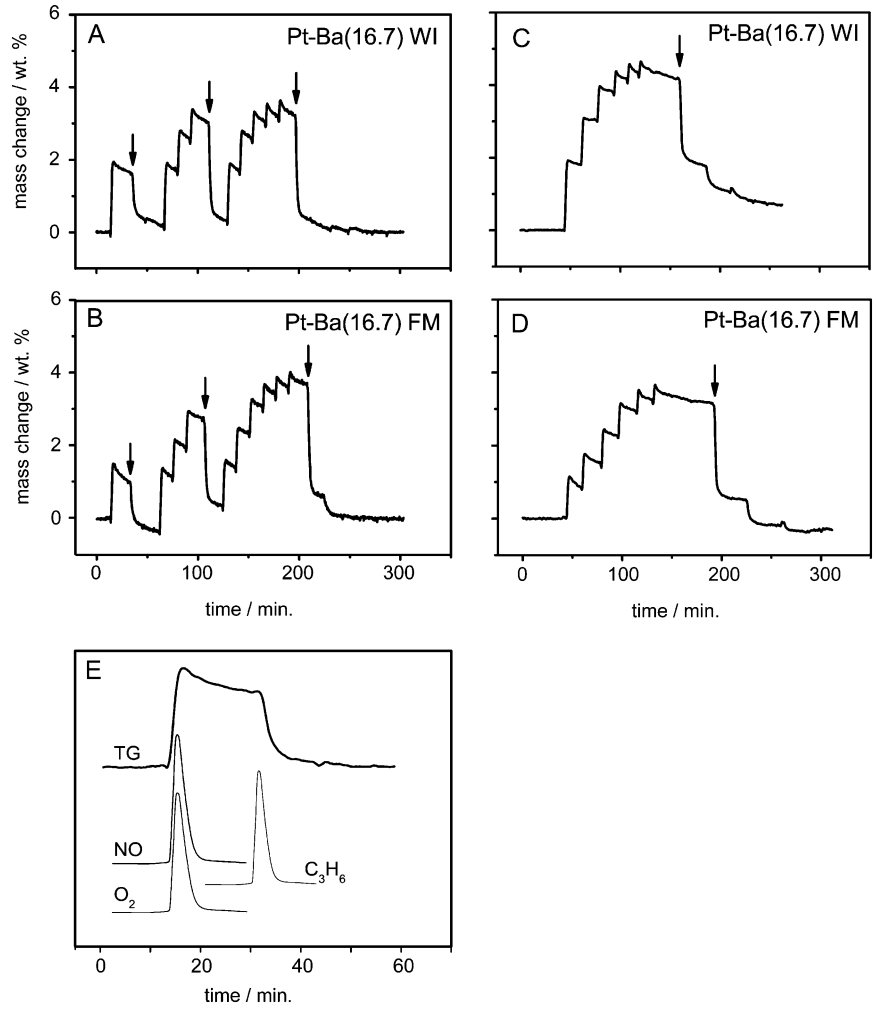

Fig. 13. NO_x storage (NO/O_2 pulses) and reduction (C_3H_6 pulses): in atmosphere of pure He (A and B) and in 8000 ppm O_2/He (C and D) at 300 °C. TG curve indicates the mass change (wt%) due to contribution of both simultaneous reactions: the uptake of NO_x and evolution of CO_2, arrows indicate the first pulse of C_3H_6 after each storage step. (E) depicts the mass changes occurring during injection NO/O_2 and propene.

the formation of traces of previously absent HT-$BaCO_3$ (peak centered at ca. 900 °C, bottom right).

4. Discussion

The buildup and thermal stability of Ba-containing phases resulting from the decomposition of $Ba(Ac)_2$ supported on alumina and platinum/alumina are strongly influenced by the interfaces with the alumina support and platinum [15,16,18]. In previous work [15], we showed that calcination of the WI catalysts at 500 °C results in the formation of two types of barium carbonates with different thermal stabilities: LT-$BaCO_3$, decomposing between 400 and 800 °C, and HT-$BaCO_3$, having bulk-like properties and decomposing at temperatures above 800 °C. Remaining Ba-containing species were in the form of BaO [$Ba(OH)_2$] confined to the interface with the alumina support. We showed that the NO_x storage occurrs mainly on active LT-$BaCO_3$ and on BaO being in an intimate contact with the support, and that the less active HT-$BaCO_3$ phase, more abundant at high Ba loading, decreases the NO_x storage efficiency due to diffusional limitations [16].

The present study compares new flame-derived catalysts (FM catalysts) to conventional catalysts prepared by wet impregnation (WI catalysts). The major benefit from applying a two-nozzle FSP process for Pt–Ba/Al_2O_3 preparation is that formation of the bulk-like HT-$BaCO_3$ phase can be greatly suppressed up to high Ba loadings.

The conventional single-nozzle FSP method led to formation of amorphous Ba species, showing very poor NO_x storage activity. The two-nozzle FSP process was developed with the goal of forming crystalline $BaCO_3$ and Al_2O_3 nanoparticles well-mixed at the nanolevel [23]. The FM catalysts have significantly different structure than the WI catalysts.

4.1. Morphology of the differently prepared catalysts

The absence of pores, characteristic of FM nanosized particle structure, allowed better stability of the catalyst surface area with increasing Ba loading (Figs. 1 and 2). Increasing the Ba content did not result in clogging of the pores of the support,

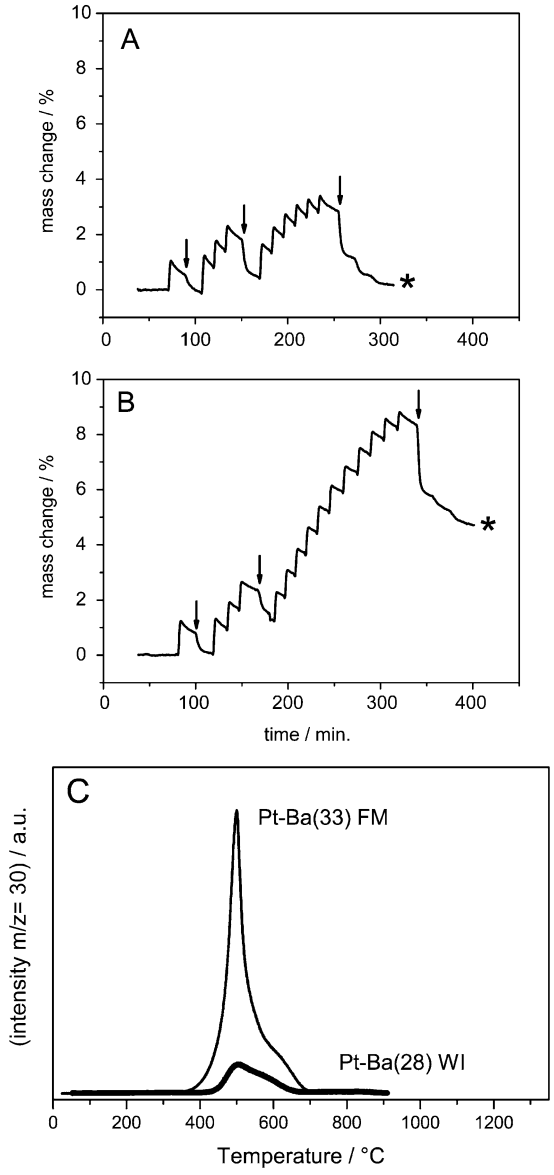

Fig. 14. TG traces obtained during NSR over highly Ba-loaded WI Pt–Ba(28) (A) and FM Pt–Ba(33) (B) catalysts (arrows indicate the first pulse of C_3H_6 after each storage step): corresponding TPRD NO evolution profiles for both samples taken at point marked by asterisks are shown in C.

as was observed with the WI catalysts. On the other hand, in the FM catalysts the surface area of Al_2O_3 was only slightly covered by Ba species, resulting in a lower Ba/Al_2O_3 interface, limited to the contact area between individual primary Ba-containing and Al_2O_3 particles.

Increasing the Ba loading had different effects in the FM and WI catalysts. In the FM catalysts, the number of nanosized Ba-containing particles continuously increased, whereas in the WI catalysts, after an initial progressive support coverage up to ca. 16 wt% Ba, the Ba-containing domains grew in thickness (Fig. 3). Finally, it is also important to stress that in the WI catalysts, the uncovered alumina surface area progressively decreased with increasing Ba loading, whereas in the FM catalysts the alumina particles still exposed a relatively large alumina surface area even at high Ba loadings.

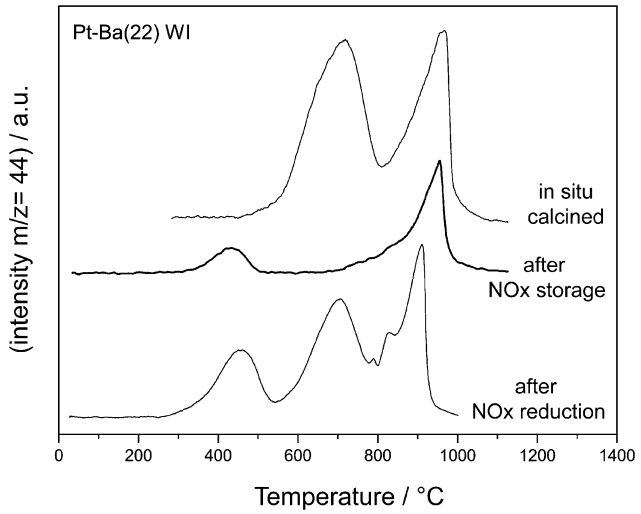

Fig. 15. CO_2 evolution profiles recorded during decomposition of $BaCO_3$, present in the samples after calcination, NO_x storage and NO_x reduction, respectively, of WI Pt–Ba(22) catalyst.

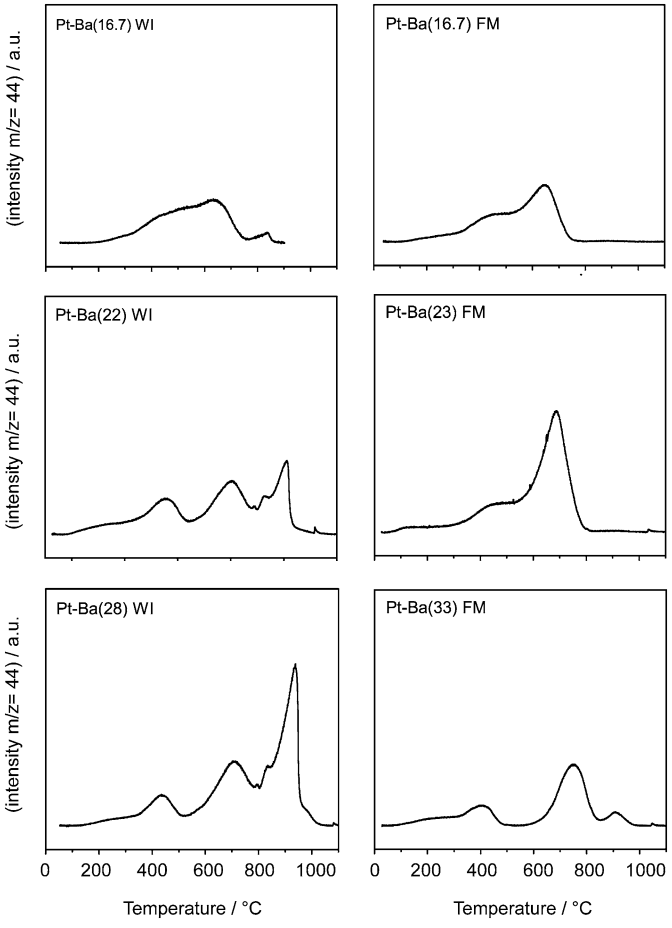

Fig. 16. TPRD CO_2 evolution profiles of decomposition of $BaCO_3$ formed during reduction by C_3H_6 of $Ba(NO_3)_2$ formed during NO_x storage on differently loaded WI and FM samples.

A simplified schematic presentation summarizing the main morphological differences between the FM and WI catalysts, as evidenced by TEM and ESI analysis (Fig. 3), along with the

related distribution of the Ba-containing species as a function of Ba loading, is shown in Scheme 1.

Pt particles in the FM and WI catalysts show different adsorption behavior of CO, as revealed by in situ DRIFTS analysis during CO chemisorption (Fig. 5). The different intensities of Kubelka–Munk-transformed signals characteristic of linear CO (L-CO, 1970, 2016, 2060, and 2076 cm^{-1}) [36,38] and bridge CO (B-CO, ca. 1800 cm^{-1}) [38] observed for the FM and WI samples (Fig. 5) indicate structural differences of the platinum component probably arising from different interfacial contacts (alumina, barium carbonate). Interestingly, we have not observed CO chemisorption over Pt-free Ba/Al_2O_3 samples, which stands in contrast to signals assigned to CO adsorption on BaO (signals in the range of 2100–1700 cm^{-1}) [10]. However, it should be noted that in [10] the $Pt–Ba/Al_2O_3$ samples were prepared using different precursors most probably affording a higher concentration of BaO. Bands at 1790–1801 cm^{-1} (Fig. 5) were present in Ba-free Pt/Al_2O_3 and in all Ba-containing samples (not shown). Prinetto et al. assigned bands at frequencies 1750–1850 cm^{-1} to "organic-like" carbonates originating from CO_2 coordinated to alumina [36], whereas Szailer et al. assigned bands at 1782–1824 cm^{-1} to NO adsorbed on precious metal particles [39]. Apparently, in both investigations, the samples were not prereduced before CO exposure, whereas when samples were pretreated, bands at ca. 1800 cm^{-1} were typically assigned to bridge CO adsorbed on Pt [38]. These different observations indicate that CO chemisorption results may depend strongly on the pretreatment conditions used for the Pt–Ba/alumina catalysts, and that rigorous comparison of results is thus biased for differently pretreated samples.

Using DRIFTS-derived stoichiometry factors, CO:Pt, to calculate Pt dispersion by means of CO chemisorption, we obtained 66% for the Pt–Ba(4.5), 28% for Pt–Ba(16.7), and 23% for Pt–Ba(28) WI catalysts, whereas for corresponding FM catalysts, the dispersions were 35 and 41, and 45% for Pt–Ba(33). These findings confirm that the influence of Ba loading on Pt dispersion depends on the preparation method [23,39–41]. In WI catalysts, the highest CO chemisorption, and consequently Pt dispersion, is reached with the lowest Ba-loaded Pt–Ba(4.5) sample [40,42]. This may be traced to the fact that in wet-chemical catalyst preparation, Ba is deposited over Pt/Al_2O_3, which may lead to progressive coverage of some Pt sites with increasing Ba loading [36].

On the other hand, in FM material, the combustion of a solution containing both Pt and Ba precursors at different concentration results in a more uniform Pt dispersion that is less dependent on Ba loading. Eventually, the formation of barium carbonates limits the growth of Pt particle size, favoring high Pt dispersion at higher Ba loading [23]. Interestingly, at low Ba loading, the Pt dispersion in the WI catalyst was almost double that in corresponding FM materials. This may be attributed to partial entrapping of Pt inside the Ba particles.

The Pt dispersion values for FM catalysts reported here are somewhat lower than those reported previously [23]. This is due to the fact that in the previous work, the standard Pt dispersion measurement method was applied [43,44]. This method was optimized for binary systems like Pt/Al_2O_3. The present DRIFTS studies of CO adsorption indicate that this method is inappropriate for more complex catalytic systems containing a high concentration of carbonates, decomposing well above 400 °C. The commonly applied reduction pretreatments in H_2 result in a water–gas shift reaction between H_2 and CO_2 stemming from decomposing $BaCO_3$, causing CO to remain on the catalyst surface. On the other hand, the pretreatment cannot be performed at temperatures above 500 °C due to possible sintering of Pt particles. Therefore, the CO chemisorption procedure adopted here has been optimized to limit the influence of carbonates present in these catalysts. Finally, it is noteworthy that the improved method for determining Pt dispersion used in this work confirms the general trend toward correlation between Ba loading and Pt dispersion observed previously for FM catalysts [23].

4.2. Stability and distribution of supported $BaCO_3$ phases

As is clear from the preceding discussion, the formation of barium carbonate phases depends on the catalyst preparation method. In the WI catalysts, the primary phase resulting from precursor decomposition was $BaCO_3$, which partly decomposes in BaO due to its low thermal stability. The relative ratio of BaO and LT-$BaCO_3$ species depended on the Ba loading. At very low Ba loading, most Ba-containing species were in intimate contact with the support, leading to high instability of the $BaCO_3$ thus formed, which decomposes completely into active BaO (see Fig. 8). Increasing the Ba loading led to increased thickness of the barium phase, characterized by weaker interaction with the support and a slightly higher thermal stability (LT-$BaCO_3$). Note that prolonged exposure to ambient atmosphere led at room temperature to partial transformation of the very active BaO into LT-$BaCO_3$, as can be clearly seen in Figs. 7 and 8 (single point). Above a Ba loading of ca. 16 wt%, the relative concentration of LT-$BaCO_3$ in WI catalysts was constant, and a new, thermally more stable HT-$BaCO_3$ phase was formed.

In FM catalysts, the primary phase after precursor combustion was BaO, which progressively formed $BaCO_3$ phases with varying thermal stabilities during cooling in the CO_2-rich atmosphere surrounding the flame. Note that in this case the interface of the Ba component with Al_2O_3 was significantly smaller than in the WI materials, which in turn limited the influence of the support on the properties of the newly formed $BaCO_3$ phase. However, the presence of alumina had a significant influence on the size of the BaO nanoparticles. Flame-made barium carbonate prepared in the absence of alumina resulted in much larger (100×50 nm), bean-shaped particles [34] than those obtained in the present study (ca. 30 nm; see Fig. 3). Moreover, unsupported FM $BaCO_3$ showed high thermal stability, comparable to that of bulk-like material. In summary, we can state that the $BaCO_3$ found in $Pt–Ba/Al_2O_3$ FM catalysts decomposed very similarly to LT-$BaCO_3$ contained in the WI catalyst, whereas unsupported FM $BaCO_3$ decomposed as bulk-like HT-carbonate at temperatures above 800 °C [34]. The high CO_2 concentration during flame synthesis (FM catalysts) resulted in higher concentration of LT-$BaCO_3$ at the expense of active

BaO, which was more abundant in the corresponding WI catalysts with the same Ba loading.

4.3. NO_x storage

The different distributions of BaO, LT-$BaCO_3$, and HT-$BaCO_3$ in WI and FM catalysts significantly affected NO_x storage capacity at high Ba loading, as illustrated in Fig. 12. The NO_x storage efficiency in high Ba-loaded samples was higher in the FM catalysts than in the corresponding WI catalysts (Figs. 9 and 12), where the bulk-like HT-$BaCO_3$ was less active and caused diffusional limitations for Ba loadings higher than Pt–Ba(22) [16].

At low Ba loadings in WI catalysts, two phases contributed to the storage of NO_x species: very active BaO formed by decomposition of LT-$BaCO_3$ and nondecomposed LT-$BaCO_3$. In FM catalysts, the main phase contributing to NO_x storage at all Ba loadings was LT-$BaCO_3$. Its thermal properties were very similar to properties of this phase in WI samples, and its complete consumption during NO_x storage was proven by CO_2 evolution profiles recorded during TPRD after exposure to NO/O_2 pulses (not shown). Note that in FM catalysts, the majority of active Ba was in the form of $BaCO_3$ (Fig. 11); the remaining BaO was mostly inactive as it was trapped in the core of the Ba-containing particles and covered by a layer of $BaCO_3$. Active BaO was present in the WI catalysts; in the FM samples, it was transformed into LT-$BaCO_3$ due to exposure to high CO_2 concentrations in the preparation process and the lower interaction of the Ba-containing phase with the alumina support, influencing the stability of the carbonate phases.

Finally, it should be stressed that the NO_x storage tests were performed with a model-type exhaust gas mixture that did not contain CO_2, H_2O, and SO_2 as real exhaust gases do. It is well known that these components can affect NO_x storage and reduction in various ways [8]. Thus a final assessment concerning the NO_x storage efficiency of the differently prepared catalysts can be given only after corresponding studies are conducted with real exhaust gases. Such studies, including in situ characterization of the catalysts, are presently underway in our laboratories.

4.4. Reduction of stored NO_x-containing species

The WI and FM catalysts showed similar activity for the reduction of stored NO_x by propene up to the highest Ba-loaded samples (Fig. 13). At high Ba loading and complete saturation with NO_x, both the WI and FM catalysts showed a somewhat reduced activity compared to the standard Pt–Ba(16.7) samples. The decrease in activity was more pronounced with FM Pt–Ba(33) (Fig. 14). This difference in reduction activity compared with the standard Pt–Ba(16.7) samples was most prominent when maximal NO_x storage was reached (i.e., during the final cycle of NO/O_2 pulses), indicating a direct influence of the concentration of NO_x-containing species on the reduction activity of the catalyst. The injection of a single pulse of C_3H_6 after a specified number of NO/O_2 pulses indicated that the reduction activity was affected by the amount of stored NO_x species. The chemistry ruling the reduction of stored NO_x species is a matter of debate; diverse mechanisms, which are not discussed here, have been proposed [8,45]. Recently, Nova et al. [46] showed how reduction of stored nitrates under isothermal conditions on Pt–Ba/Al_2O_3 occurs via a Pt-catalyzed reaction that does not involve thermal decomposition of stored NO_x.

A feasible explanation for the lower reduction activity of the highly Ba-loaded catalysts (Fig. 14) is that the formation of a larger amount of $Ba(NO_3)_2$ leads to surface reconstruction due to the higher molar volume of that compound compared with $BaCO_3$ [47]. This process may lead to blocking of Pt active sites and, consequently, limited reduction activity of the catalyst.

In a detailed study on the reduction of NO by propene over Pt–Ba/Al_2O_3 catalysts, Konsolakis and Yentekakis showed how Ba overpromotion leads to an excessive concentration of surface nitrates, affecting the number of Pt active sites available for reactants [42]. Moreover, they reported Ba-promoting NO adsorption on Pt sites at the expense of propene, which favors NO reduction up to ca. 15 wt% of Ba, whereas higher Ba loadings seem detrimental to the reduction activity of Pt. Similar behavior was observed by Anderson et al. [48], who reported that activation of propene over Pt–Ba/Al_2O_3 catalysts was disfavored by stored NO_x species. Decreased NSR efficiency with increasing Ba loading was also reported by Castoldi et al. [40], who found decreased selectivity in highly Ba-loaded WI Pt–Ba/Al_2O_3 catalyst during the reduction with H_2 of previously stored NO_x species [46].

4.5. Regeneration of supported $BaCO_3$ phases after NSR

An important aspect of the NSR concept is the possibility of perpetually cycling the storage and reduction steps. It seemed important to verify whether the distribution of the $BaCO_3$ phases, described in detail in our previous studies [15,16], is regenerated after repeated NSR cycles in both FM and WI catalysts. The results depicted in Fig. 16 confirm the stability of the particular $BaCO_3$ phase distribution present in FM catalysts, characterized by a high concentration of LT-$BaCO_3$ and absence of HT-$BaCO_3$. Stability was also observed for WI samples (Figs. 15 and 16). The amount of $BaCO_3$ decomposing below 800 °C was determined from the $m/z = 44$ traces presented in Fig. 16. These values were similar for samples with the same Ba loading (e.g., for samples with 16.7 wt% Ba, 41% and 48% of the total Ba-loaded for WI and FM samples, respectively). This indicates that despite the different phase compositions in fresh WI and FM catalysts, after one cycle of NO_x storage reduction, the relative amount of LT-$BaCO_3$ was similar in the two catalysts, due to the partial transformation of active BaO into LT-$BaCO_3$ in the WI catalysts. The only exception to this was the highly Ba-loaded FM Pt–Ba(33) sample, which showed slight high-temperature CO_2 evolution during TPRD (Fig. 16), indicating probable formation of HT-$BaCO_3$. This finding suggests the partial conversion of LT-$BaCO_3$ into less efficient HT-$BaCO_3$ and is in line with the interconversion between the two different alumina-supported Ba-NO_x species recently described by Chen et al. [13]. Although this phenomenon needs further investigation, particularly with tests using

real exhaust gases, it must be taken into account as a possible origin of the Pt–Ba/Al_2O_3 aging phenomena and a possible cause of NSR catalyst deactivation. Consequently, a worthwhile goal is to improve the efficiency and stability of NSR catalysts by maximizing and stabilizing the LT-$BaCO_3$ phase and minimizing the formation of the less efficient HT-$BaCO_3$ phase.

5. Conclusion

The aim of the present work was to develop a novel Pt–Ba/Al_2O_3 NSR catalyst with minimal HT-$BaCO_3$ content but high LT-$BaCO_3$ content. Active Ba in NO_x storage in WI catalysts was previously found to be in the form of LT-$BaCO_3$ and BaO in intimate contact with support [15,16]. Preparation of FM catalysts using a two-nozzle FSP process proved useful for reaching this goal. A series of FM Pt–Ba/Al_2O_3 catalysts with Ba loading (4.5–33 wt%) was prepared, and the structural properties and NO_x storage reduction behavior of these catalysts were compared to those of standard Pt–Ba/Al_2O_3 catalysts prepared by wet impregnation (WI catalysts) using model-type exhaust gas mixtures. Varying relative abundances of BaO, LT-$BaCO_3$, and HT-$BaCO_3$ were found depending on the preparation method used. High Ba-loaded FM catalysts were virtually free of HT-$BaCO_3$ and exhibited improved NO_x storage capacity compared to WI catalysts with the same Ba content.

DRIFTS investigation of CO chemisorption on the FM and WI catalysts revealed that the preparation method and the Ba loading affects the distribution of CO adsorption sites, indicating significant structural differences of the Pt particles, caused by the preparation route and the Ba loading. Reduction tests showed some limitation of the activity of high Ba-loaded FM catalysts, possibly related to the partial blocking of active Pt sites at high loading of $Ba(NO_3)_2$. Preliminary tests based on prolonged NSR cycling indicated the partial transformation of some active LT-$BaCO_3$ to HT-$BaCO_3$, which may be a phenomenon that needs to be taken into account when explaining the deactivation of NSR catalysts.

Acknowledgments

Financial support was provided by ETH (TH-proposal 2/03-2). The authors thank Dr. Frank Krumeich for performing the electron microscopy investigations and Dr. Davide Ferri for helping with the DRIFTS studies.

References

[1] E. Jobson, Top. Catal. 28 (2004) 191.
[2] J. Kaspar, P. Fornasiero, N. Hickey, Catal. Today 77 (2003) 419.
[3] N. Miyoshi, S. Matsumoto, K. Katoh, T. Tanaka, J. Harada, N. Takahashi, K. Yokota, M. Sugiura, K. Kasahara, SAE Tech. Paper 950809 (1995).
[4] N. Takahashi, H. Shinjoh, T. Iijima, T. Suzuki, K. Yamazaki, K. Yokota, H. Suzuki, N. Miyoshi, S. Matsumoto, T. Tanizawa, T. Tanaka, S. Tateishi, K. Kasahara, Catal. Today 27 (1996) 63.
[5] W. Bogner, M. Kramer, B. Krutzsch, S. Pischinger, D. Voigtlander, G. Wenninger, F. Wirbeleit, M.S. Brogan, R.J. Brisley, D.E. Webster, Appl. Catal. B 7 (1995) 153.
[6] E. Fridell, H. Persson, B. Westerberg, L. Olsson, M. Skoglundh, Catal. Lett. 66 (2000) 71.
[7] S. Matsumoto, CATTECH 4 (2000) 102.
[8] W.S. Epling, L.E. Campbell, A. Yezerets, N.W. Currier, J.E. Parks, Catal. Rev. 46 (2004) 163.
[9] W.S. Epling, J.E. Parks, G.C. Campbell, A. Yezerets, N.W. Currier, L.E. Campbell, Catal. Today 96 (2004) 21.
[10] P.T. Fanson, M.R. Horton, W.N. Delgass, J. Lauterbach, Appl. Catal. B 46 (2003) 393.
[11] J. Szanyi, J.H. Kwak, D.H. Kim, S.D. Burton, C.H.F. Peden, J. Phys. Chem. B 109 (2005) 27.
[12] J. Szanyi, J.H. Kwak, J. Hanson, C.M. Wang, T. Szailer, C.H.F. Peden, J. Phys. Chem. B 109 (2005) 7339.
[13] X. Chen, J. Schwank, J. Li, W.F. Schneider, J. Goralski, T. Christian, P.J. Schmitz, Appl. Catal. B 61 (2005) 189.
[14] S. Elbouazzaoui, E.C. Corbos, X. Courtois, P. Marecot, D. Duprez, Appl. Catal. B 61 (2005) 236.
[15] M. Piacentini, M. Maciejewski, A. Baiker, Appl. Catal. B 59 (2005) 187.
[16] M. Piacentini, M. Maciejewski, A. Baiker, Appl. Catal. B 60 (2005) 265.
[17] M. Piacentini, M. Maciejewski, T. Burgi, A. Baiker, Top. Catal. 30–31 (2004) 71.
[18] M. Piacentini, M. Maciejewski, A. Baiker, Appl. Catal. B 66 (2006) 126.
[19] L. Mädler, KONA 22 (2004) 107.
[20] L. Mädler, H.K. Kammler, R. Mueller, S.E. Pratsinis, J. Aerosol Sci. 33 (2002) 369.
[21] R. Strobel, W.J. Stark, L. Mädler, S.E. Pratsinis, A. Baiker, J. Catal. 213 (2003) 296.
[22] R. Strobel, S.E. Pratsinis, A. Baiker, J. Mater. Chem. 15 (2005) 605.
[23] R. Strobel, L. Mädler, M. Piacentini, M. Maciejewski, A. Baiker, S.E. Pratsinis, Chem. Mater. 18 (2006) 2532.
[24] E.P. Barrett, L.G. Joyner, P.P. Halenda, J. Am. Chem. Soc. 73 (1951) 373.
[25] B.C. Lippens, J.H.d. Boer, J. Catal. 4 (1965) 319.
[26] W. Grogger, F. Hofer, P. Warbichler, G. Kothleitner, Microsc. Microanal. 6 (2000) 161.
[27] A. Bourane, O. Dulaurent, D. Bianchi, Langmuir 17 (2001) 5496.
[28] K. Kawasaki, T. Kodama, H. Miki, T. Kioka, Surf. Sci. 64 (1977) 349.
[29] K.A. Thrush, J.M. White, Appl. Surf. Sci. 24 (1985) 108.
[30] M. Maciejewski, C.A. Müller, R. Tschan, W.D. Emmerich, A. Baiker, Thermochim. Acta 295 (1997) 167.
[31] M. Eberhardt, R. Riedel, U. Gobel, J. Theis, E.S. Lox, Top. Catal. 30–31 (2004) 135.
[32] J. Dawody, L. Eurenius, H. Abdulhamid, M. Skoglundh, E. Olsson, E. Fridell, Appl. Catal. A 296 (2005) 157.
[33] T. Nishino, T. Sakurai, N. Ishizawa, N. Mizutani, M. Kato, J. Solid State Chem. 69 (1987) 24.
[34] R. Strobel, M. Maciejewski, S.E. Pratsinis, A. Baiker, Thermochim. Acta 446 (2006) 23.
[35] L. Lietti, P. Forzatti, I. Nova, E. Tronconi, J. Catal. 204 (2001) 175.
[36] F. Prinetto, G. Ghiotti, I. Nova, L. Lietti, E. Tronconi, P. Forzatti, J. Phys. Chem. B 105 (2001) 12732.
[37] I. Nova, L. Castoldi, F. Prinetto, V. Dal Santo, L. Lietti, E. Tronconi, P. Forzatti, G. Ghiotti, R. Psaro, S. Recchia, Top. Catal. 30/31 (2004) 181.
[38] A. Bourane, O. Dulaurent, D. Bianchi, J. Catal. 196 (2000) 115.
[39] T. Szailer, J.H. Kwak, D.H. Kim, J.C. Hanson, C.H.F. Peden, J. Szanyi, J. Catal. 239 (2006) 51.
[40] L. Castoldi, I. Nova, L. Lietti, P. Forzatti, Catal. Today 96 (2004) 43.
[41] K.S. Kabin, R.L. Muncrief, M.P. Harold, Y.J. Li, Chem. Eng. Sci. 59 (2004) 5319.
[42] M. Konsolakis, I.V. Yentekakis, J. Catal. 198 (2001) 142.
[43] J. Freel, J. Catal. 25 (1972) 149.
[44] H.L. Gruber, Anal. Chem. 34 (1962) 1828.
[45] R. Burch, J.P. Breen, F.C. Meunier, Appl. Catal. B 39 (2002) 283.
[46] I. Nova, L. Lietti, L. Castoldi, E. Tronconi, P. Forzatti, J. Catal. 239 (2006) 244.
[47] U. Tuttlies, V. Schmeisser, G. Eigenberger, Top. Catal. 30/31 (2004) 187.
[48] J.A. Anderson, B. Bachiller-Baeza, M. Fernandez-Garcia, Phys. Chem. Chem. Phys. 5 (2003) 4418.